Suppressed radiation-induced dynamic recrystallization in CrFeCoNiCu high-entropy alloy

Jinyeon Kim [a,b,1], Jong Wook Lim [a,c,1], Joon Kon Kim [a], Do Hyang Kim [c], Eun Soo Park [b,*], Hye Jung Chang [a,d,*]

[a] Advanced Analysis Center, Korea Institute of Science and Technology, Seoul 02792, Republic of Korea
[b] Department of Materials Science and Engineering, Seoul National University, Seoul 08826, Republic of Korea
[c] Center for Noncrystalline Materials, Yonsei University, Seoul 03722, Republic of Korea
[d] Division of Nano & Information Technology, KIST School, University of Science and Technology, Seoul 02792, Republic of Korea

ABSTRACT

We report a map of irradiation-induced recrystallization and polygonization in a CrFeCoNiCu high-entropy alloy obtained by a precession electron diffraction technique. This orientation map enables the visualization of depth-dependent recrystallization at a glance and reveals the effects of irradiation dose and material entropy. Discontinuous dynamic recrystallization preferentially occurs near the surface, where the irradiation dose is low, but radiation-enhanced diffusion dominantly occurs leading to dislocation climb even at room temperature. Interestingly, in the high-entropy phase with a relatively low stacking fault energy, discontinuous dynamic recrystallizastion is suppressed due to the lower stored energy and grain boundary diffusivity compared low-entropy one.

Materials under irradiation are subject to dynamic force conditions that drive alloys into non-equilibrium configurations by ballistic diffusion [1] and radiation-enhanced diffusion [2]. In particular, radiation-enhanced diffusion results from the supersaturation of vacancies and self-interstitial atoms produced by atomic displacement under irradiation, which accelerate solute diffusion and thus drive the system toward a new equilibrium state. The evolution of radiation-induced dislocations into dislocation cell structures with low-angle boundaries (LABs) and their further recrystallization with high-angle grain boundaries (HAGBs) have been investigated in various materials [3–9], mainly utilizing transmission electron microscopy (TEM) [3–6].

The detailed mechanism of deformation-induced recrystallization has been systematically elucidated, whereas the majority of studies on irradiation-induced recrystallization have been phenomenological due to the following experimental difficulties. i) Unlike deformation-induced recrystallization, radiation-induced recrystallization occurs locally only at the surface and strongly depends on the depth due to differing dose levels and defect mobility along the radiation direction. Thus, it is necessary to understand the overall microstructural evolution considering the specimen depth. However, the plane-view microstructures prepared by conventional TEM sampling methods like chemical jet polishing or Ar ion milling with a controlled sampling depth hardly represent a depth-sensitive surface structure. ii) To identify the recrystallization mechanism, the misorientation angles between grains and even in grains should be quantitatively measured with a high spatial resolution across a wide region. Electron backscattered diffraction (EBSD) has commonly been applied to simultaneously map the crystal orientation of materials on the microscale and measure the misorientation between grains [10]. However, the spatial resolution of EBSD is insufficient to resolve ion irradiation-induced dislocation cell structures or recrystallized fine grains that are concentrated only at the surface. On the other hand, TEM analysis using selected area diffraction patterns (SADPs) [5,6] or convergent-beam Kikuchi patterns is useful for studying the misorientation of fine grains and visualizing subgrains. However, point-by-point TEM analysis is time- and labor-consuming and lacks a reliable statistical quantity. Thus, obtaining a comprehensive understanding of the misorientation angles in a wide area is somewhat difficult. To overcome these limitations, we applied a recently developed analytical method for TEM-based orientational imaging using precession electron diffraction (PED) [11,12] to study the recrystallization mechanism of materials under irradiation.

Recently, it was reported that high-entropy alloys (HEAs) exhibit excellent phase stability and enhanced damage tolerance, which are attractive properties for structural materials under extreme environments [13–15] and nuclear materials [16–21]. Interestingly, under ion irradiation, the increased compositional complexity in HEAs results in suppressed damage accumulation [16,17], mitigated segregation [18–20], and restrained swelling [18,21]. Among HEA systems, the $Cr_{20}Fe_{20}Co_{20}Ni_{20}Cu_{20}$ alloy, a composite consisting of a CrFeCoNi-rich dendritic high-entropy (HE, 22.8 at.%Cr-22.9 at.% Fe-23.2 at.%Co-20.7 at.% Ni-10.4 at.%Cu) phase and Cu-rich interdendritic low-entropy (LE, 3.0 at.%Cr-3.4 at.%Fe-3.3 at.%Co-8.2 at.%Ni-82.1 at.%Cu) phase, was selected as a model system in this study. Based on the grain orientation maps obtained from plane and cross-sectional views of the target alloy after irradiation at room temperature, the ion irradiation-induced recrystallization mechanism was carefully examined. This new approach applying an advanced characterization technique to reveal the irradiation-induced recrystallization mechanism is expected to represent a step forward in related research fields.

The target alloy was fabricated into a plate with dimensions of 2.5 mm × 6 mm × 50 mm by arc melting and subsequent suction casting under a Ti-gettered Ar atmosphere. The alloy was irradiated with 9.5 MeV Cu^{4+} ions and 13.3 MeV Cu^{6+} ions at room temperature using a 2 MeV tandem accelerator at the Korea Institute of Science and Technology (KIST), and temperature is set to 10°C using a water-cooling system to prevent a beam heating effect (for details, see Fig. S3 in Supplementary Information). The irradiation damage determined by SRIM calculations [22] was converted into displacement per atom (dpa) under full damage cascade mode with displacement energies of 40 eV for Cr, Fe, Co, and Ni and 30 eV for Cu [23]. At a depth of 1.5 μm, the fluence was 5.0×10^{14} ions/cm² at 1 dpa and 5.0×10^{15} ion/cm² at 10 dpa for 9.5 MeV Cu ion irradiation. Cross-sectional and plane-view TEM samples were prepared using a dual-beam focused ion beam (FIB) microscope (Thermo Fisher Scientific; Helios Nanolab 600) to visualize the radiation-induced defects and recrystallization depending on the depth and investigate the recrystallization behavior across phase boundaries, respectively. Nanoscale microstructural analysis was carried out using TEM (Thermo Fisher Scientific; Tecnai F20). Crystal orientation mapping was performed by TEM using PED (NanoMEGAS) and ASTAR as the hardware and data acquisition software packages [24]. The precession angle of the electron beam was 1°, and the step size was set to 10 nm for the cross-sectional sample and 2.5 nm for the plane-view sample. The diffraction pattern at each step was recorded by an external high-speed camera and indexed automatically to the calculated diffraction pattern for a face-centered cubic (FCC) structure (Fm3m, (225)).

The calculated depth profile under the 1 dpa irradiation condition is overlaid on the bright-field (BF) TEM image in Fig. 1(a). The implanted Cu ion concentration increased gradually to a maximum at a depth of 2.6 μm, and the associated damage was expected to be most severe at approximately 2.4 μm. Beyond these maxima, the Cu concentration and damage decreased significantly and stopped at a depth of 3.0 μm, where the dark contrast caused by defects disappears in the BF-TEM image. The TEM image was obtained under the two-beam BF condition along the diffraction vector g=<200> in order to effectively observe the defects, and so the dark contrast in the image represents a large number of irradiation-induced defects. Thus, it was confirmed that the calculated damage depth was well matched to the experimental results. However, the dark contrast fades closer to the surface, where cell structure-like contrast appears. Based on the contrast in the BF-TEM image, the irradiated sample can be divided into three zones along the depth direction: grain-refined, damaged, and unaffected. Here, we focus on the grain-refined zone, where irradiation-induced subgrains evolve and recrystallization occurs.
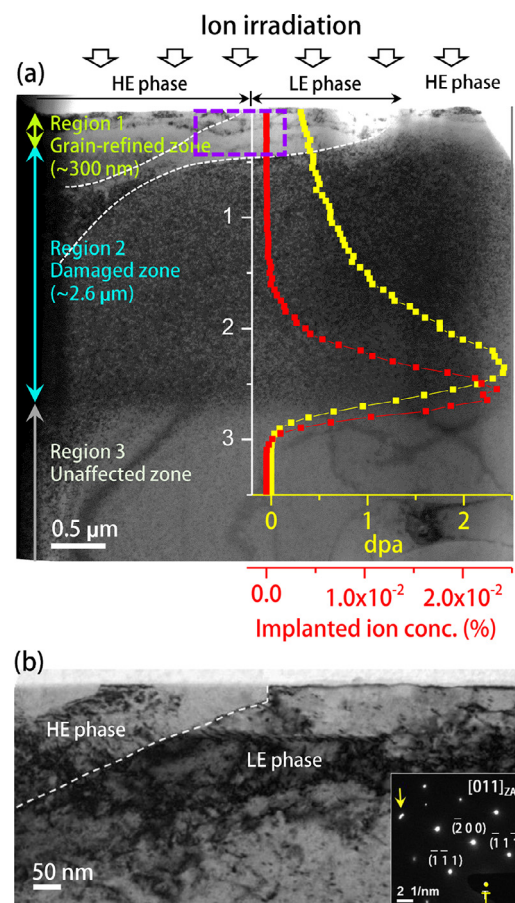
Fig. 1. (a) Cross-sectional BF-TEM image and corresponding SADPs of the CrFeCoNiCu HEA irradiated at room temperature and 13.3 MeV 1 dpa. The BF images were obtained with the two-beam condition along diffraction vector g=<200>. The crystal orientation of the HE and LE phases in this image are the same, and both have an FCC structure with similar lattice parameters. The white dashed lines indicate the phase boundaries between the HE and LE phases. The overlaid profiles show implanted Cu ion concentration and dose depending on depth. (b) Magnified image of the purple dashed box in (a). The inset SADP obtained from the LE phase shows the locally rotated crystal orientation.

Irradiation-induced subgrain formation and recrystallization occurred below 300 nm from the surface in the boundary region between LE and HE phases (purple dashed box in Fig. 1(a)). Because subgrains and recrystallization were not observed before ion irradiation (for details, see Fig. S2(a) in Supplementary information), it was realized that they are products by radiation damage. The magnified image of the cell structure and elongated or separated diffraction spots in the SADP in Fig. 1(b) imply that subgrains formed beneath the surface. However, these results are limited to showing i) how deep the subgrains formed, ii) the size and shape of the subgrains, and iii) the misorientation angles between them. Thus, the PED technique was utilized to evaluate the grain-refined zone more quantitatively.

The PED orientation map in Fig. 2(a) shows that grains nucleated preferentially near the phase boundary and surface. The misorientation angle quantitatively measured along the depth direction (from inside the sample to the surface) increased gradually in the HE phase, whereas that in the LE phase showed a stepped increase (Fig. 2(b)). Here, we differentiate recrystallized grains from polygonized subgrains by the misorientation angle and shape, where subgrains with LABs are mostly elongated. The depth of the subgrain formation was greater near the phase boundary for both phases. Approaching the surface, equiaxed grains with HAGBs occurred more frequently near the phase boundary and in the LE
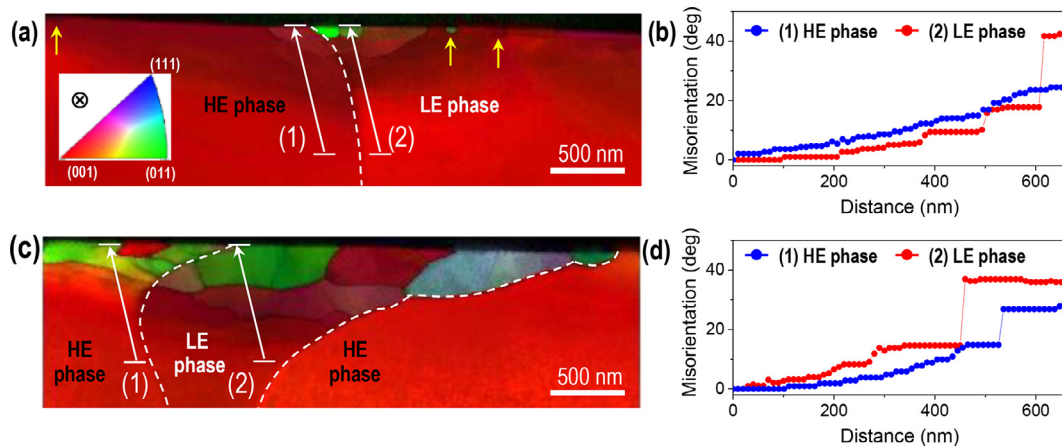
Fig. 2. (a and c) PED-based orientation maps of cross-sectional TEM samples of the CrFeCoNiCu HEA after 9.5 MeV Cu ion irradiation (1 dpa and 10 dpa) at room temperature, respectively. (b and d) Line profiles of misorientation angles along the arrows from inside the sample toward the surface in the HE phase (1) and LE phase (2) for (a) and (c), respectively.

phase, which has a lower resistance to irradiation than the HE phase.

With more severe irradiation at 10 dpa, polygonization and recrystallization began at greater depths in both the LE and HE phases, and the recrystallized grains became larger (Fig. 2(c)). This indicates that the increase in developed radiation defects under a high irradiation dose leads to an increase in radiation-enhanced diffusion. Consequently, dislocation climb is more prominent, even at room temperature [5,6,8,25], and grain nucleation and growth subsequently occur under dynamic recrystallization. Evidence for the recrystallization mechanism was found at a low irradiation dose (Fig. 2(a)). Recrystallization occurs preferentially at the surface of the phase boundary and rarely occurs at the surface away from the phase boundary. The inhomogeneous distribution of equiaxial grains with sharp boundaries can be an evidence of discontinuous dynamic recrystallization (DDRX). However, the cross-sectional view with its limited scope cannot represent the general recrystallized microstructure, and thus the microstructure along the plane view was also examined as shown in Fig. 3.

The SEM image in Fig. 3(a) shows the irradiated microstructure just below the surface. As expected from the SEM image, the development of fine grains having large HAGBs with neighbors in the LE phase was clearly visualized in the orientation map (Fig. 3(b)). On the other hand, only LABs were observed in the HE phase region. The angle between points A and B was 4°, and only a small difference in misorientation was detected between points G and H (Fig. 3(c)). On the other hand, abrupt orientation changes occurred in the LE phase. For instance, the misorientation at the phase boundary between points B and C was 27°, and the angle between points D and E was 36°. It is noteworthy that the grains with HAGBs were mostly located near the phase boundary, which is the preferred site for grain nucleation. Some sparse individual grains with HAGBs were present inside the LE phase (marked by white arrows in Fig. 3(b)), which is consistent with the analysis of the cross-sectional sample (Fig. 2(a)).

Heavy ion irradiation increases the density of point defects composed of vacancies and interstitial clusters, which develop into dislocation loops [26]; these further interact to evolve dislocations [27]. Therefore, irradiation increases the overall dislocation density and thus the stored energy in the materials. Activation of dislocation climb due to radiation-enhanced diffusion facilitates dislocation rearrangement, grain boundary movement, and further recrystallization [25].

In Fig. 4(a and b), we illustrate the radiation-induced recrystallization process in the HE and LE phases of the CrFeCoNiCu HEA
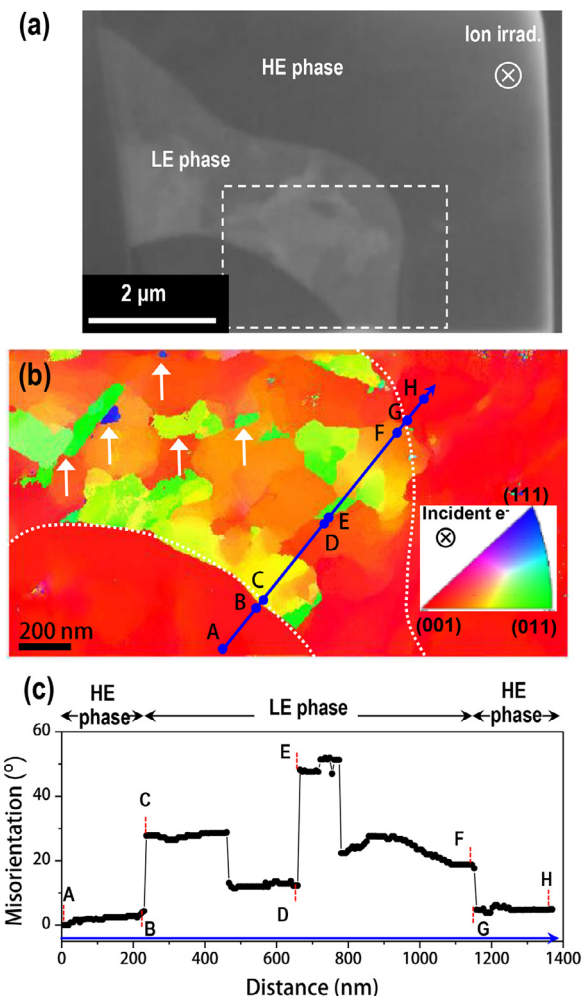
Fig. 3. (a) Plane-view SEM image of the surface of the CrFeCoNiCu HEA after 9.5 MeV Cu ion irradiation (1 dpa) at room temperature; (b) corresponding orientation map showing the subgrain structure and recrystallization; and (c) line profile of grain misorientation along the blue line across the phase boundaries in (b).

under irradiation doses of 1 and 10 dpa, respectively. In the early stage of recrystallization in both phase regions (Fig. 4(a)), recrystallized grains with equiaxial shapes containing few dislocations nucleate and grow. This occurs preferentially at the phase boundary as well as near the surface, which is evidence of DDRX. With more
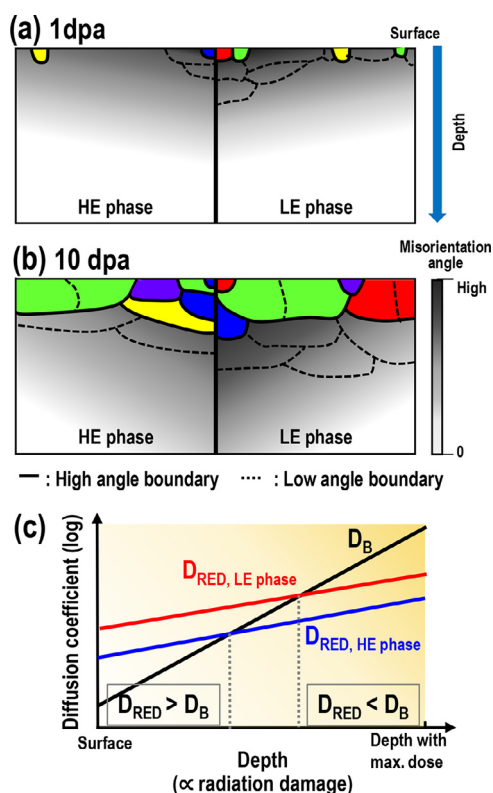
Fig. 4. Schematics of radiation-induced polygonization and recrystallization processes at (a) the initial stage after low-dose irradiation (1 dpa) and (b) the latter stage after high-dose irradiation (10 dpa). The solid (—) and dashed (—) lines represent HAGBs and LABs, respectively. (c) Schematic diagram of the relationship between depth and diffusion coefficients (D_{RED} and D_B) in the HE phase and LE phase.

severe irradiation (Fig. 4(b)), the starting depths of polygonization and recrystallization increase, and the recrystallized grains become larger due to the increase in developed radiation defects.

The phase stability of materials under irradiation is determined by the competition between ballistic diffusion (i.e., accelerating atomic mixing and vacancy–interstitial atom recombination) and radiation-enhanced diffusion (i.e., enhancing defect clustering and growth), which drives the microstructure to follow different evolutional trends [28]. First, the ballistic diffusion coefficient, D_B, is defined as $D_B=1/6R\lambda^2$ [29], where R is the dose rate and λ is the relocation distance of solute atoms. R is proportional to the irradiation dose, which increased with depth up to 2.4 μm in this study, and λ is a constant dependent on the irradiation condition. Thus, D_B increases with depth if defects are not annihilated each other. Second, the radiation-enhanced diffusivity, D_{RED}, accelerates thermodynamically driven processes which in this case promotes dynamic recrystallization. D_{RED} is defined as $D_{RED}=(c_v^{irr}/c_v^{eq})D_{th}$ [29], where c_v^{irr} is the vacancy concentration under irradiation, c_v^{eq} is the equilibrium vacancy concentration, and D_{th} is the thermal diffusion coefficient. When the defects accumulate without any reaction and do not recombine at defect sinks, c_v^{irr} is also proportional to the irradiation dose, and thus D_{RED} linearly increases with depth. The slope of D_{RED} vs. depth is smaller than that of D_B vs. depth under ion irradiation, and so D_{RED} and D_B intersect at some point with increasing depth, as shown in Fig. 4(c). Thus, because D_{RED} (defect clustering) outweighs D_B (defect random mixing) near the surface ($D_{RED}>D_B$), recrystallization and polygonization preferentially occur, and the misorientation angle also decreases with increasing depth.

DDRX in mechanical deformation is usually observed in materials with low stacking fault energies (SFEs) like Cu, Ag, and

austenitic steel [30,31]. Since the SFE of CrFeCoNi (32 mJ/m²) [32] is lower than that of pure Cu (55 mJ/m²) [33], DDRX is expected to be more favorable in the CrFeCoNi HE phase. In this study, however, the Cu-rich LE phase exhibited more significant DDRX behavior with notable grain nucleation and growth than the HE phase (Fig. 3(b)). Hence, to investigate the suppressed DDRX behavior in the HE phase, the grain nucleation and growth under dynamic recrystallization were further considered.

First, in terms of grain nucleation, the critical subgrain size (r_i) to nucleate grains is inversely proportional to the stored energy in the grains [33,34]. The higher defect formation enthalpy [35,36] and lower thermal diffusivity [37] of the HE phase result in slower energy dissipation in the cascade and enhance vacancy–interstitial atom recombination during the cascade reaction. As a result, compared with the LE phase, surviving defect clusters and their accumulation are suppressed in the HE phase. This leads to a lower $D_{RED,HE}$ (Fig. 4(c)) and reduces the stored energy, thereby suppressing the grain nucleation in dynamic recrystallization.

Second, in terms of grain growth, the grain boundary velocity (v_i) is determined by the grain boundary mobility (M_{HAG}) and the stored energy (G_i) between the grain (ρ_i) and the effective medium ($\bar{\rho}$) [33,34]. In the HE phase, the stored energy is relatively low since $D_{RED,LE}/D_B > D_{RED,HE}/D_B$, as explained above. Furthermore, according to calculations, the Ni grain boundary diffusivities in pure Cu and the CrFeCoNi alloy are 1.8×10^{-29} [32] and 1.8×10^{-42} m³/s [38], respectively. This indicates that the HE phase has a lower M_{HAG} than that of the LE phase. As a consequence, the lower stored energy in the grains and slower grain boundary migration in the HE phase result in a lower $D_{RED,HE}$ (Fig. 4(c)) and restrained grain growth in dynamic recrystallization. Thus, the lower defect density and grain boundary diffusivity suppress grain nucleation and growth in the dynamic recrystallization of the HE phase.

In summary, the cross-sectional and plane-view microstructural evolution of the CrFeCoNiCu HEA after heavy Cu ion irradiation was quantitatively investigated by PED-based orientation mapping as an advanced TEM technique. Interestingly, after irradiation at room temperature, DDRX occurs mostly near the surface where the dose is low rather than inside the sample where the dose is high due to the higher D_{RED} than D_B. Additionally, DDRX is relatively suppressed in the HE phase compared with the LE phase due to restrained grain nucleation and growth, which are related to the lower stored energy and grain boundary diffusivity. We anticipate that our approach will pave the way for understanding irradiation-induced recrystallization behavior in three dimensions and developing radiation-damage-tolerant materials for use under various extreme environments.

Data availability

The data that support the findings of this study are available from Dr. Chang (email: almacore@kist.re.kr) and Prof. Park (email: espark@snu.ac.kr) upon reasonable request.

Declaration of Competing Interest

The authors declare that they have no known competing financial interests or personal relationships that could have appeared to influence the work reported in this paper.

Acknowledgements

Supplementary materials

Supplementary material associated with this article can be found, in the online version, at doi:10.1016/j.scriptamat.2020.08.045.

References

[1] G. Martin, Phys. Rev. B 30 (1984) 1424.
[2] G. Dienes, A. Damask, J. Appl. Phys 29 (1958) 1713.
[3] H. Matzke, L. Wang, J. Nucl. Mater 231 (1996) 155.
[4] J. Kai, W. Huang, H. Chou, J. Nucl. Mater 170 (1990) 193.
[5] W. Vaidya, K. Ehrlich, J. Nucl. Mater 113 (1983) 149.
[6] E. Nesterova, V. Rybin, S. Zinkle, V. Barabash, A. Naberenkov, Plasma Dev. Oper. 2 (1994) 293.
[7] O. El-Atwani, M. Efe, B. Heim, J.P. Allain, J. Nucl. Mater. 434 (2013) 170.
[8] S. Zinkle, G. Kulcinski, L. Mansur, J. Nucl. Mater. 141–143 (1986) 188.
[9] T. Sonoda, M. Kinoshita, I.L.F. Ray, T. Wiss, H. Thiele, D. Pellottiero, V.V. Rondinella, H. Matzke, Nucl. Instrum. Meth. B 191 (2002) 622.
[10] L. Brewer, D. Field, C. Merriman, in: Electron Backscatter Diffraction in Materials Science, Springer, 2009, pp. 251–262.
[11] E. Rauch, M. Véron, Mater. Charact. 98 (2014) 1.
[12] V. Hrkac, N. Wolff, V. Duppel, I. Paulowicz, R. Adelung, Y.K. Mishra, L. Kienle, Appl. Microsc. 49 (2019) 1.
[13] B. Gludovatz, A. Hohenwarter, D. Catoor, E.H. Chang, E.P. George, R.O. Ritchie, Science 345 (2014) 1153.
[14] F. Otto, A. Dlouhy, C. Somsen, H. Bei, G. Eggeler, E. George, Acta Mater. 61 (2013) 5743.
[15] H. Oh, S. Kim, K. Odbadrakh, W. Ryu, K. Yoon, S. Mu, F. Körmann, Y. Ikeda, C. Tasan, D. Raabe, T. Egami, E. Park, Nat. Commun 10 (2019) 2090.
[16] Y. Zhang, G. Stocks, K. Jin, C. Lu, H. Bei, B. Sales, L. Wang, L. Beland, R. Stoller, G. Samolyuk, M. Caro, A. Caro, W. Weber, Nat. Commun. 6 (2015) 8736.
[17] F. Granberg, K. Nordlund, M. Ullah, K. Jin, C. Lu, H. Bei, L. Wang, F. Djurabekova, W. Weber, Y. Zhang, Phys. Rev. Lett. 116 (2016) 135504.
[18] N. Kumar, C. Li, K. Leonard, H. Bei, S. Zinkle, Acta Mater. 113 (2016) 230.
[19] C. Lu, T. Yang, K. Jin, N. Gao, P. Xiu, Y. Zhang, F. Gao, H. Bei, W. Weber, K. Sun, Y. Dong, L. Wang, Acta Mater. 127 (2017) 98.
[20] M. He, S. Wang, S. Shi, K. Jin, H. Bei, K. Yasuda, S. Matsumura, K. Higashida, I. Robertson, Acta Mater. 126 (2017) 182.
[21] C. Lu, L. Niu, N. Chen, K. Jin, T. Yang, P. Xiu, Y. Zhang, F. Gao, H. Bei, S. Shi, M. He, I. Robertson, W. Weber, L. Wang, Nat. Commun. 7 (2016) 13564.
[22] J. Ziegler, J. Biersack, U. Littmark, SRIM – the Stopping and Range of Ions in Matter, Ion Implantation Press, 2008.
[23] R. Stoller, M. Toloczko, G. Was, A. Certain, S. Dwaraknath, F. Garner, Nucl. Instrum. Methods Phys. Res. Sect. B 310 (2013) 75.
[24] D. Viladot, M. Veron, M. Gemmi, F. Peiro, J. Portillo, S. Estrade, J. Mendoza, N. Llorca-Isern, S. Nicolopoulos, J. Microsc. 252 (2013) 23.
[25] D. Mordehai, G. Martin, Phys. Rev. B 84 (2011) 014115.
[26] K. Sickafus, E. Kotomin, B. Uberuaga, Radiation Effects in Solids, Springer Science & Business Media, 2007.
[27] S. Mahajan, B. Eyre, Acta Mater. 122 (2017) 259.
[28] S. Shu, N. Almirall, P. Wells, T. Yamamoto, G. Odette, D. Morgan, Acta Mater. 157 (2018) 72.
[29] G. Was, Fundamentals of Radiation Materials Science: Metals and Alloys, Springer, 2016.
[30] T. Sakai, A. Belyakov, R. Kaibyshev, H. Miura, J. Jonas, Prog. Mater. Sci. 60 (2014) 130.
[31] K. Huang, R. Logé, Mater. Des. 111 (2016) 548.
[32] S. Divinski, J. Ribbe, G. Schmitz, C. Herzig, Acta Mater. 55 (2007) 3337.
[33] D. Cram, X. Fang, H. Zurob, Y. Bréchet, C. Hutchinson, Acta Mater. 60 (2012) 6390.
[34] D. Cram, H. Zurob, Y. Brechet, C. Hutchinson, Acta Mater 57 (2009) 5218.
[35] S. Middleburgh, D. King, G. Lumpkin, M. Cortie, L. Edwards, J. Alloys Compd. 599 (2014) 179.
[36] S. Foiles, M. Baskes, M. Daw, Phys. Rev. B 33 (1986) 7983.
[37] J. Lee, H. Oh, E. Park, Appl. Phys. Lett. 109 (2016) 061906.
[38] M. Vaidya, K. Pradeep, B. Murty, G. Wilde, S. Divinski, Sci. Rep 7 (2017) 12293.